TITLE:

Experimental investigation of a new 3D printed Wells turbine under dynamic stall conditions for wave energy conversion

AUTHOR NAMES AND AFFILIATIONS:

Michele Stefanizzi[a], Marco Torresi[a], Sergio Mario Camporeale[a]

[a]Department of Mechanics, Mathematics and Management (DMMM), Polytechnic University of Bari, Via Re David 200, 70125, Bari, Italy; michele.stefanizzi@poliba.it; marco.torresi@poliba.it; sergio.camporeale@poliba.it

CORRESPONDING AUTHOR:

Michele Stefanizzi

Mail: michele.stefanizzi@poliba.it

Address: Re David 200, 70125, Bari, Italy

Phone: +393381456833

ABSTRACT:

Marine energy still plays a marginal role in the current global energy scenario, despite the incessant effort by research for more than thirty years in the exploitation of the so-called blue energy. Nevertheless, thanks to a raising awareness of the gravity related to the climate changes, energy poverty and energy security, the Nations are expressing a common willingness to increase also the global installed capacity by ocean energy. Among the wide range of marine technologies, wave energy harvesting can play a significant role in view of its potential and Oscillating Water Column (OWC) systems, coupled with Wells turbines, can be considered among the most mature wave energy technology. Due to the oscillating nature of the flow rate in this kind of applications, Wells turbines are affected by dynamic stall, which has significant effects in terms of performance, vibration, noise and structural integrity of the turbine.

Actually, during dynamic stall, the Wells turbine experiences evident high frequency torque fluctuations which overlay on the typical hysteresis loop, mainly during flow deceleration. The amplitudes of these fluctuations are damped as the flow rate decreases toward reattachment. Often these fluctuations are not evident because hysteresis loops are usually provided with phase-averaged data, which can significantly smoothen or even conceal them. Indeed, it is difficult to find in the literature high frequency torque measurements able to show these fluctuations. With the aim to better investigate this phenomenon, this work proposes a new 3D-printed monoplane Wells turbine, which has been tested at the open wind tunnel of the Polytechnic University of Bari, Italy. The interest of the experimental campaign has been mainly focused on the effects of main parameters of the oscillating flow rate (mean frequency, frequency amplitude and period of the vector control drive of the squirrel cage blower) on the performance of the machine. The machine has been firstly investigated in steady state, then under dynamic stall working conditions. As a result, unsteady torque fluctuations occur during the flow deceleration till the flow reattachment; moreover, this phenomenon is intensified as the amplitude of the oscillating flow rate increases and the wave period decreases. Hence, detecting these oscillations can be relevant in the turbine design phase to enhance the structural strength of the turbine. Moreover, it has been found that this unsteady behavior is due neither to the mass flow rate crossing the turbine nor to the stagnation pressure drop, but only to the detachment of vortices generated from the leading edge and travelling along the suction side of the blade.

KEYWORDS:

Wells Turbine; Wave Energy; OWC; Ocean Energy; Marine Energy; Blue economy.

Experimental investigation of a new 3D printed Wells turbine under dynamic stall conditions for wave energy conversion

Michele Stefanizzi[a*], Marco Torresi[a], Sergio Mario Camporeale[a]

[a]*Department of Mechanics, Mathematics and Management (DMMM), Polytechnic University of Bari, Via Re David 200, 70125, Bari, Italy;*
**michele.stefanizzi@poliba.it; marco.torresi@poliba.it; sergio.camporeale@poliba.it*

Abstract

Marine energy still plays a marginal role in the current global energy scenario, despite the incessant effort by research for more than thirty years in the exploitation of the so-called blue energy. Nevertheless, thanks to a raising awareness of the gravity related to the climate changes, energy poverty and energy security, the Nations are expressing a common willingness to increase also the global installed capacity by ocean energy.

Among the wide range of marine technologies, wave energy harvesting can play a significant role in view of its potential and Oscillating Water Column (OWC) systems, coupled with Wells turbines, can be considered among the most mature wave energy technology. Due to the oscillating nature of the flow rate in this kind of applications, Wells turbines are affected by dynamic stall, which has significant effects in terms of performance, vibration, noise and structural integrity of the turbine.

Actually, during dynamic stall, the Wells turbine experiences evident high frequency torque fluctuations which overlay on the typical hysteresis loop, mainly during flow deceleration. The amplitudes of these fluctuations are damped as the flow rate decreases toward reattachment. Often these fluctuations are not evident because hysteresis loops are usually provided with phase-averaged data, which can significantly smoothen or even conceal them. Indeed, it is difficult to find in the literature high frequency torque measurements able to show these fluctuations. With the aim to better investigate this phenomenon, this work proposes a new 3D-printed monoplane Wells turbine, which has been tested at the open wind tunnel of the Polytechnic University of Bari, Italy. The interest of the experimental campaign has been mainly focused on the effects of main parameters of the oscillating flow rate (mean frequency, frequency amplitude and period of the vector control drive of the squirrel cage blower) on the performance of the machine. The machine has been firstly investigated in steady state, then under dynamic stall working conditions. As a result, unsteady torque fluctuations occur during the flow deceleration till the flow reattachment; moreover, this phenomenon is intensified as the amplitude of the oscillating flow rate increases and the wave period decreases. Hence, detecting these oscillations can be relevant in the turbine design phase to enhance the structural strength of the turbine. Moreover, it has been found that this unsteady behavior is due neither to the mass flow rate crossing the turbine nor to the stagnation pressure drop, but only to the detachment of vortices generated from the leading edge and travelling along the suction side of the blade.

Keywords: Wells Turbine; Wave Energy; OWC; Ocean Energy; Marine Energy; Blue economy.

1. Introduction

Nowadays the effects of climate change are so tangible that they can no longer be ignored and direct counter actions cannot be postponed anymore. The widespread adoption of renewables and related technologies represents an essential solution to fight worrisome issues such as climate change, energy poverty and energy security. One of the latest report by the International Renewable Energy Agency (IRENA) outlines that CO_2 emissions related to the energy production sector increased by 1.3% annually, on average, between 2014 and 2019 [1]. Despite the sharp trend inversion caused by the COVID-19 pandemic (almost 8% lower than in 2019, i.e. 31.5 Gt $CO_{2,eq}$ in the 2020), global CO_2 emissions due to energy production rebounded in 2021. Indeed, they rose by 1.2 billion tons in 2021 [2] [3] [4].

In this scenario, the recent COP 26 has represented an important milestone in giving a strong signal with an even more explicit desire to global zero net emissions by 2050 and to limit the increase in temperatures to 1.5 °C. In order to achieve these ambitious goals, Nations are called to accelerate the phase-out of coal, curtail deforestation, speed up the switch to electric vehicles and encourage investment in renewables [5][6][7].

Regarding renewables, it must be said that a continuous and ongoing effort is made by Nations in developing and installing more and more renewables based technologies for electric generation. Indeed, as reported in figure 1, the renewable share of annual capacity expansion has increased in the last 20 years, starting from 25% in 2001 and reaching an overall of 82% in 2020. Moreover, the same trend has been showed in terms of renewable capacity addition with a record level of 260 GW added in 2020 and a global renewable generation capacity of about 2.8 TW [1]. As depicted in figure 2, the key role among renewables share is played by hydropower with a capacity of 1.2 TW (43% of the global total). Hydropower is followed by solar and wind energy with their share of about 26% each. The remaining part consists of 127 GW provided by bioenergy, 14 GW by geothermal, plus 500 MW of ocean energy [8].

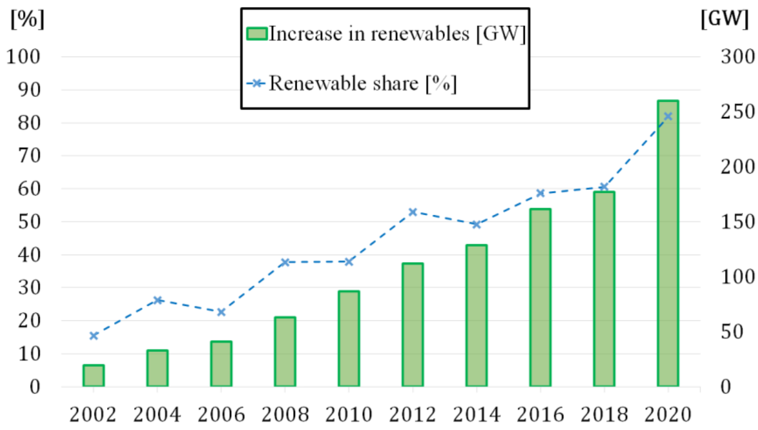

Fig. 1. Trend of share and annual capacity addition of renewable based power.

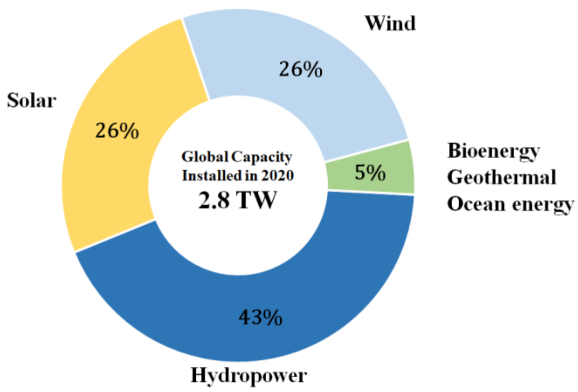

Fig. 2. Renewable generation capacity by energy source.

1.1. Ocean Energy Status

Unlike other renewable sources, which are currently used on a large scale, the marine energy sector shows a significant resource potential that has not yet been exploited. Indeed, the potential of ocean energy resources can range from 40000 TWh to 130000 TWh per year and depends on the technology involved, as illustrated in Figure 3 [9], [10].

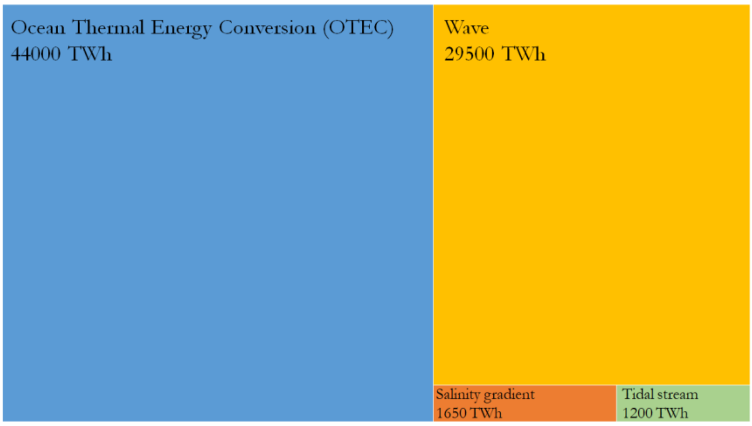

Fig. 3. Ocean energy resource potential.

Actually, although Academia and Industry are working on the use of marine energy for more than thirty years, the so-called *blue energy* is not yet an established reality in the global energy mix. Indeed, most of the technologies show a low Technology Readiness Level (TRL) value and are still in the R&D stage [9]. As shown in figure 4, the most developed technologies are related to tidal and wave energy in terms of global installed capacity, which totally reaches about 530 MW.

Moreover, it must be considered that few countries have this energy resource available and can become leading actors in the economic scenario related to the ocean energy. In addition to the European countries (e.g., Finland, France, Ireland, Italy, Portugal, Spain, Sweden), the UK, Australia, Canada and the USA are the major players in the blue energy market, thanks to the biggest amount of projects designed and deployed [9].

In order to increase the global installed capacity, the European Union has proposed the *European offshore renewable energy strategy* with the aim to reach at least 1 GW of tidal and wave energy by 2030 and 40 GW by 2050 [12]. Obviously, this development must also be economically feasible, for instance guaranteeing an appropriate levelized cost of energy (LCOE) [11]. According to current estimates, the LCOE for tidal energy is estimated between USD 0.20-0.45/kWh and for wave energy between USD 0.30-0.55/kWh, but they are expected to decrease as the technology becomes more and more established. For example, the LCOE of tidal and wave energy based technologies are forecast to reach about USD 0.11/kWh and USD 0.165/kWh by 2030, respectively [12][13][14].

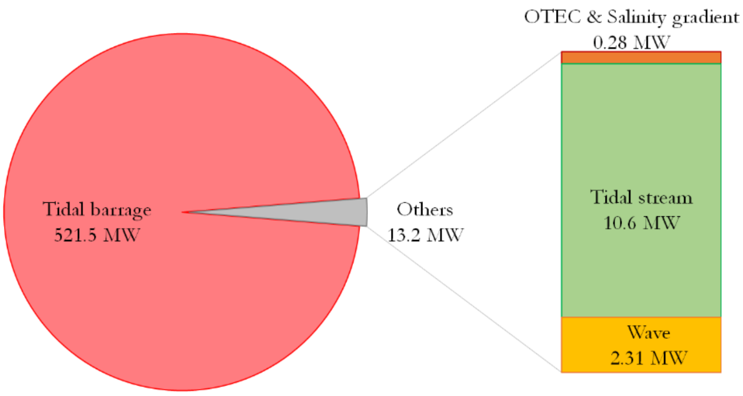

Fig. 4. Total ocean energy deployment.

1.2. Oscillating Water Column (OWC) systems and Wells Turbine

Wave energy is suitable for those areas characterized by advantageous conditions of wave height, wave speed and wavelength. Typically, these physical properties maximize the exploitable power in areas at latitudes within 30 and 60 degrees and in deep water (greater than 40 m). Despite the seasonal variation, waves can be considered a valid energy source, since it is possible to accurately forecast them with the current level of technology.

Among the wide range of technologies, Oscillating Water Column (OWC) devices can be considered among the most mature ones for wave energy harvesting [15], showing a TRL equal to 8 [9]. Basically, OWC systems consist of an *ad hoc* designed chamber, which is semi-submerged in the water. The periodic motion of the waves causes an oscillating movement of the water contained in the structure. This effect, in turn, alternately compresses and expands the volume of overlying air, which is conveyed into a duct containing the Power Take-Off (PTO) system. Since the air flow direction alternatively changes, OWC systems require self-rectifying machines, for instance Wells turbines [16]. Indeed, the Wells turbine shows its distinctive feature in rotating in the same direction irrespective of the oscillating air flow direction. This can be explained by the operating principle behind the development of this machine, which dates back to 1980's [17]. As depicted in figure 5, its blades with symmetrical airfoils, staggered at a 90 deg angle, allow the tangential force always directed in the same direction.

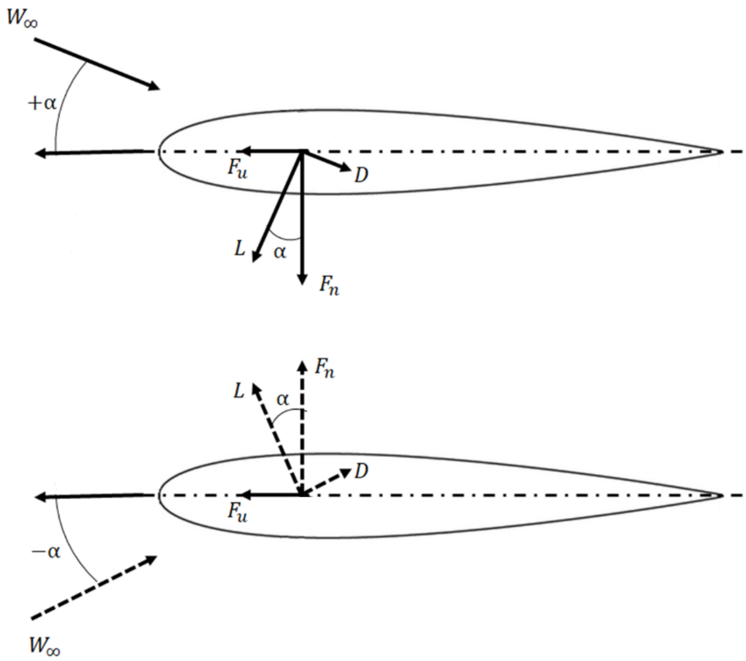

Fig. 5. Forces acting on a typical Wells turbine blade under oscillating flow rate.

As an example of an OWC technology-based power plant, Mutriku wave energy plant, located in the bay of Mutriku (Spain), can be mentioned. The power plant is able to provide a total rated power of about 296 kW thanks to 16 OWC chambers, each of them coupled with a 18.5 kW self-rectifying Wells turbine. As reported in [18][19], the operation of this kind of plants is not easy, due do the high energy content of the area. Indeed, from the construction (in 2006) to the inauguration (in 2011), the plant suffered severe damages due to strong storms. During its first five years of operation, it supplied over 1.3 GWh of power to the grid. In 2020, the Mutriku plant produced a cumulative total of 2 GWh [20] [21]. Falcão et al. [22] presented a comprehensive review on OWC technology, analyzing all the power plants that have been built since the 2000s.

However, Wells turbine shows a series of drawbacks, such as low aerodynamic efficiency, narrow operating range, poor self-starting characteristics, high axial force coefficient and low tangential force coefficient [23]. For this reason, a significant number of numerical and experimental works have been carried out to improve the performance of Wells turbines. Gato et al. [24] carried out an experimental campaign on two types of blades: the former with constant thickness and the latter with a variable thickness by keeping unchanged the solidity, the number of blades and chord length. Moreover, it was investigated the beneficial effect of guide vanes to remove flow swirl at the exit. Also Takao et al. [25] conducted a similar analysis. Indeed, they considered a blade with a thickness increasing from the hub to the tip (in details, NACA0015 at hub, NACA0020 at midspan and NACA0025 at tip). From experimental tests, both efficiency and stall operating conditions were improved thanks to this geometry with respect to the conventional one. Torresi et al. [26] performed a detailed CFD analysis on a Wells Turbine by comparing numerical results with experimental ones. This analysis showed how the blade tip gap was a key affecting parameter for the overall performance in terms of torque coefficient and efficiency.

Among the most recent studies, Abassi et al. [23] numerically investigated the effects of addition of micrometer protrusions similar to shark skin on blades of a Wells turbine. As results, covered blades caused 18.36% increase in the torque and an increase of the turbine efficiency of 2.3%. Kotb et al. [27] studied the effect of Gurney flap geometry on the Wells turbine performance. In details, their study outlined how a circular cavity in a rectangular Gurney flap allows to increase the torque coefficient of the machine of about 27% with respect to the conventional Wells turbine. Geng et al. [28] carried out an audit and quantification of losses that occur inside the Wells turbine, highlighting how the secondary flow loss coupled together with friction losses present the greatest weight. Ciappi et al. [29][30] proposed wave-to-wire models with an interesting compromise between accuracy and computational costs. Gurnari et al. [31] performed unsteady numerical simulations to study the interaction between waves and a U-shaped OWC breakwater equipped with a Wells turbine, focusing on energy conversion process form wave to the turbine power output. Shaaban et al. [32] numerically investigated the effects of a Venturi duct geometry in order to enhance the Wells turbine performances, reaching up to 9% with the optimized geometry.

Alves et al. [33] carried out experimental tests on a Wells turbine with specially designed guide vanes. The presence of the guide vanes was found to increase the peak efficiency by seven percentual points, while reducing (for fixed rotational speed) the damping provided by the turbine. The addition and the design of the guide vanes was investigated also by Mahrooghi et al. [34] by using hybrid artificial neural fuzzy networks. Starzmann and Carolus [35] proposed a novel blade design method based on skewed blades. After numerical and experimental analysis, they found that optimal backward/forward blade skew from hub to tip delayed the onset of stall by increasing the range of unstalled operation with respect to the conventional straight blade design. Kumar et al. [36] proposed a new design of the Wells turbine blade, able to increase the performance range by 22% and the power by 97%, but decreasing the efficiency by 7.7% due to increased pressure drop. This changing in performance was due to a solution with a blade characterized by a variable-thickness, a curved radial edge blade and an extended trailing edge.

Although a Wells turbine could reach high efficiencies, its performance is strongly affected by dynamic stall phenomenon, which involve its typical hysteretic behavior during high amplitude flow rate oscillations. Actually, a considerable number of works have been performed with the aim to analyze both experimentally and numerically the hysteresis loop of a Wells turbine during unsteady working conditions. For instance, Paderi et al. [37] and Puddu et al. [38] found out that hysteresis is more evident during outflow and negligible during the inflow period. Setoguchi et al. [39] carried out a numerical investigation to understand the influence of blade thickness, solidity and mounting angle. This analysis found out that the hysteresis loop was less affected by blade thickness than the other two parameters. Thakker and Abdulhadi [40][41] performed an experimental and a numerical campaign on a Wells turbine under unsteady conditions by focusing on the effects of blade profile and solidity. Kim et al. [42] focused on the tip clearance and the hub-to-tip ratio, showing how the former (specifically its increase) has a greater effect on the hysteresis loop than the latter.

All these works focused on hysteresis phenomenon in working conditions not characterized by the so-called deep stall. Indeed, as depicted in figure 6, when the machine experiences strong variations of flow rate, the stall occurs with a clockwise hysteresis loop. Indeed, figure 6 shows typical performance curves of a Wells turbine in terms of non-dimensional parameters, which will be discussed in detail in the next sections (i.e., the torque coefficient, T^*, vs. the flow coefficient, U^*). This phenomenon is due to the flow separation, close to the tip, on the blade suction side, as evidenced by experiments performed by Setoguchi et al. [43] and Kinoue et al. [44]. Moreover, Ghisu et al. [45] argued that the cause of the hysteresis loop was related to the compressibility effect in the OWC system. M'zoughi et al. [46] proposed a rotational speed control based on artificial neural network in order to avoid stall operating conditions of a Wells turbine installed in a OWC.

Actually, during stall the Wells turbine experiences evident torque fluctuations, which overlay on the typical hysteresis loop, mainly during flow deceleration. The amplitudes of these fluctuations are damped as the flow rate decreases toward reattachment. Often these fluctuations are not evident because hysteresis loops are usually provided with phase-averaged data, which can significantly smoothen or even conceal them. Indeed, it is difficult to find in the literature high frequency torque measurements able to show these fluctuations.

With the aim to better investigate this phenomenon, this work proposes a new 3D-printed monoplane Wells turbine, which has been tested at the open wind tunnel of the Polytechnic University of Bari, Italy. The interest is mainly focused on the effects of frequency and amplitude of the oscillating flow rate on the performance of the machine. Hence, detecting these oscillations can be relevant in the turbine design phase to enhance the structural strength of the turbine.

In this framework, the work initially gives an overview on renewable energy mix, focusing on the current blue energy scenario and its related technologies. In details, OWC systems and Wells turbine are particularly investigated (section 1). Then, section 2 describes the Wells turbine designed and tested at the GaVe lab of the Polytecnic University of Bari, which is described in section 3. Afterwards, section 4 and 5 illustrate the experimental campaign voted to characterize the turbine under steady and dynamic stall flow conditions, respectively. Finally section 6 ends up the work with a sum up and the discussion of the results.

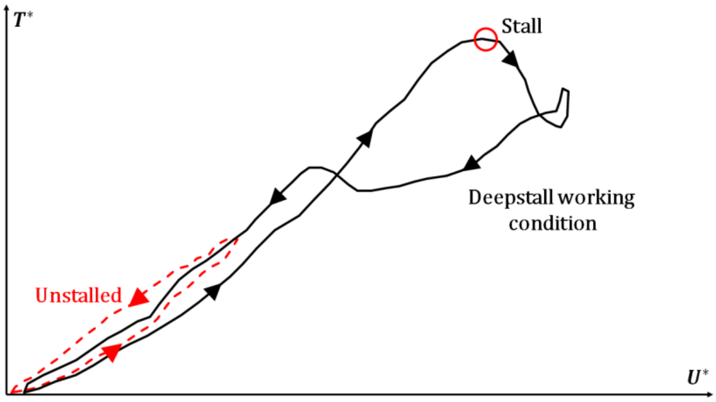

Fig. 6. Comparison of a hysteresis loop in unstalled and deep stall condition.

2. The Wells turbine

Figure 7 shows a view of the 3D printed Wells turbine under investigation, whose design parameters (i.e., turbine solidity, hub-to-tip ratio and blade airfoil) have been chosen in order to design a prototype suitable for a 1:10 scaled model of a REWEC (Resonant Wave Energy Converter) breakwater, located in Reggio Calabria, Italy [47]. As previously mentioned, the turbine rotor has been created by means of a 3D printer (named Stratasys Object30 Pro) and it is made of VeroClear material, a transparent PolyJet photopolymer.

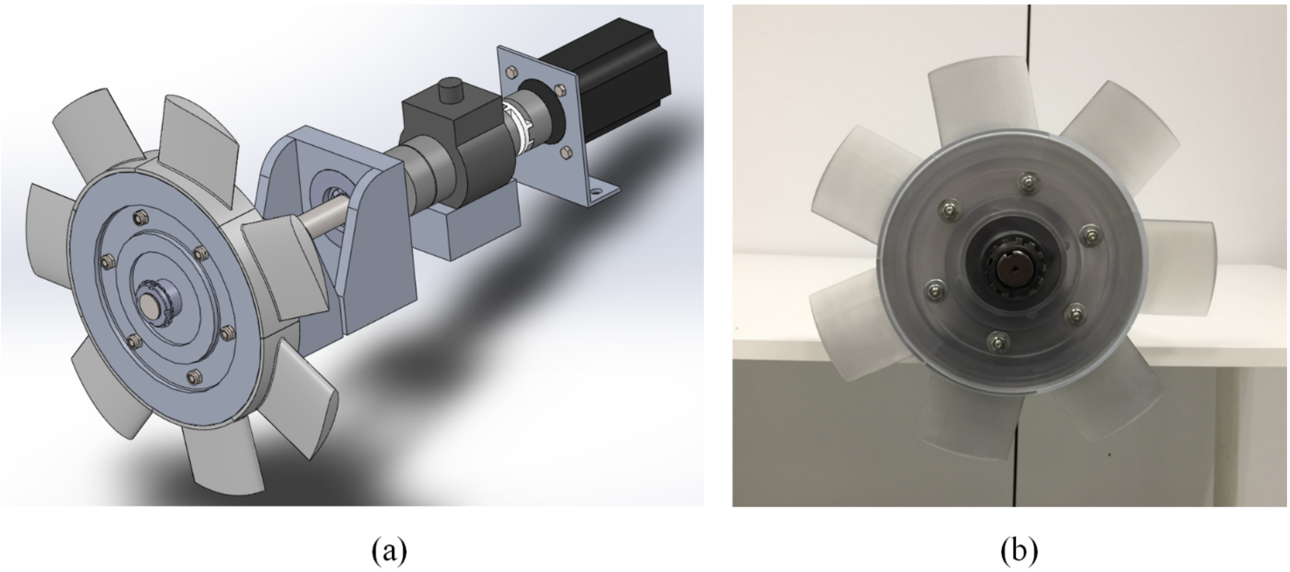

Fig. 7. 3D model of the designed Well turbine (a); Manufactured 3D-printed model of the Wells turbine (b).

Figure 8 represents the technical drawing of the designed blade, characterized by a constant chord (c = 74 mm) and a NACA0015 profile. In details, hub and tip radii are 100 mm and 155 mm, respectively. Finally, the rotor is constituted by 7 blades ($N_b = 7$). Hence, the prototype shows a solidity s = 0.6466, which is defined according to equation 1.

$$s = \frac{N_b\, c}{2\pi R_{mid}} \tag{1}$$

where R_{mid} is the mid span radius, defined as follows:

$$R_{mid} = \frac{(1+h)R_{tip}}{2} \tag{2}$$

with $h = {R_{hub}}/{R_{tip}}$ the hub-to-tip ratio.

Performance of a Wells turbine can be evaluated by means of non-dimensional parameters. These parameters are the flow coefficient, U^*, the stagnation pressure drop coefficient, Δp^*, the torque coefficient, T^*, and the efficiency, η.

Specifically, the flow coefficient, U^*, is defined as the ratio between the bulk axial velocity of the air, evaluated upstream the turbine, and the peripheral velocity evaluated at the blade tip (see equation 3).

$$U^* = \frac{V}{\omega R_{tip}} \tag{3}$$

Equation 4 defines the stagnation pressure drop coefficient, Δp^*, as follows:

$$\Delta p^* = \frac{\Delta p_0}{\rho_{air}\, \omega^2\, R_{tip}^2} \tag{4}$$

with ρ_{air} and Δp_0 the air density and the stagnation pressure drop, respectively.

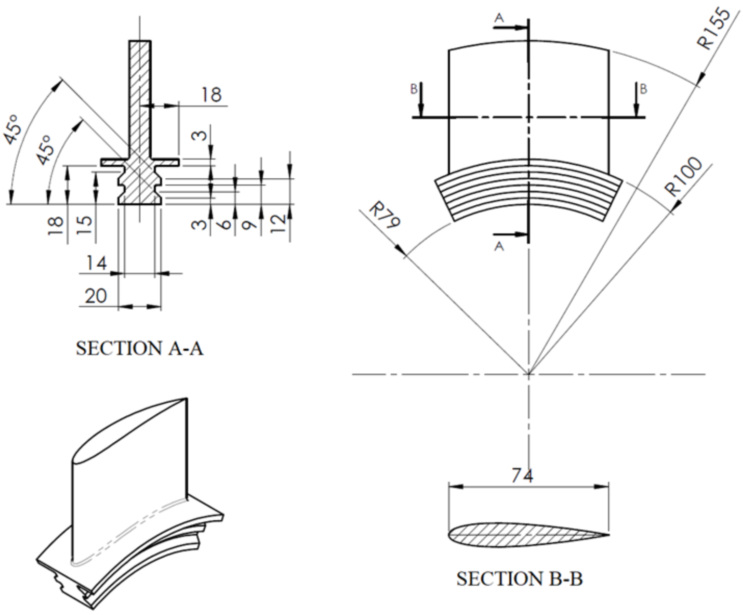

Fig. 8. Technical drawing of the blade of the Wells turbine under investigation

The torque coefficient, T^*, is determined by equation 5:

$$T^* = \frac{T_t}{\rho_{air}\, \omega^2\, R_{tip}^5} \tag{5}$$

Where T_t is the aerodynamic turbine torque, i.e. the torque applied by the flow to the blade. As explained in a previous work [48][49], this torque is different from that measured by means of the torque meter, $T_{Torque\,meter}$, because of the aerodynamic windage and mechanical frictions. From an experimental point of view, it is possible to assess these two contributions. Precisely, the turbine is motored by an electric motor without air flow in a wind tunnel, which will be described in the next section. The absence of air is achieved by keeping the blower off. In this way, the torque meter is able to measure $T_{Torque\,meter}^{no\,flow}$, which include not only windage and friction losses, but also the drag of blades. Indeed, without air flow (i.e., $V = 0$ m/s), the angle of attack of the flow is equal to 0 deg. The torque related to the drag, $T_t^{no\,flow}$, was derived from 3D CFD simulations performed in previous works by Torresi et al. [26]. Hence, the aerodynamic turbine torque, T, can be computed as follows:

$$T_t = -T_{Torque\,meter} + T_{Torque\,meter}^{no\,flow} - T_t^{no\,flow} \tag{6}$$

Once computed T_t, the efficiency of the turbine, η, can be evaluated by means of equation 7, where P_P is the available pneumatic power, $P_P = Q\Delta p_0$.

$$\eta = \frac{\omega T}{P_P} \tag{7}$$

3. The test rig

Figure 9 shows the view of the test rig employed in the experimental campaign. Fundamentally, it consists of an open circuit wind tunnel (of the suction type) and is located in the GaVe lab at the Polytechnic University of Bari, Italy. The Wells turbine is installed inside the first duct (3.5 m long), which is constituted of a first convergent duct (with a length of L = 1 m, inlet and outlet diameters D_{IN} = 445 mm, D_{OUT} = 314 mm, respectively). Then, a settling chamber (1.5 m long, 1.0 m wide and 1.0 m high) with an inner honeycomb structure is installed with the aim to cancel tangential velocity components. This chamber is connected to the blower by means of a 4.5 m long duct, where the flow rate measurements are performed according to the ISO 5147-1 standard. Indeed, this part is equipped with a section where it is possible to install different orifice plates chosen as pressure differential devices. Each plate is characterized by a diameter ratio, β, (precisely 0.2, 0.3, 0.4, 0.5, 0.6 and 0.75) in order to reduce measurement uncertainty for different flow rates. The relative pressure upstream the orifice is measured by means of a Honeywell 163PC01D36 amplified pressure transducer (pressure range of ±5″ H_2O – accuracy ± 2%). In addition, the differential pressure value across the orifice is measured by means of a Honeywell 164PC01D76 amplified pressure transducer. This device is characterized by a pressure range of 0÷5″ H_2O and accuracy ± 2%. A squirrel cage blower (model A0 112M – 4 by ELPROM) is installed at the end of the wind tunnel. The blower has the key role to generate the oscillating air flow in order to simulate the typical operating conditions of an OWC system. It is driven by an AC electric motor (2 poles, nominal power equal to 4.1 kW at 1430 rpm), which in turn is powered by a vector control drive, model V1000 by Omron (nominal power of 5.5 kW).

Regarding the equipment useful to measure the performances of the Wells turbine, a second Honeywell 163PC01D36 amplified pressure transducer is used to measure the stagnation pressure drop across the turbine. In order to measure the pressure difference, one side of the transducer is connected at a pressure tap in the settling chamber, whereas the other side is open to the atmosphere. Moreover, a P-Series SanyoDenky Servo Motor with an embedded encoder is coupled to the turbine as electric generator. In addition, the torque is measured by the torquemeter T22/5NM by HBM (T_{max} = 5 Nm, accuracy class 0.5). Finally, an in-house Supervisor Control and Data Acquisition (SCADA) developed in the NI LabVIEW® environment manages and controls the entire rig during tests.

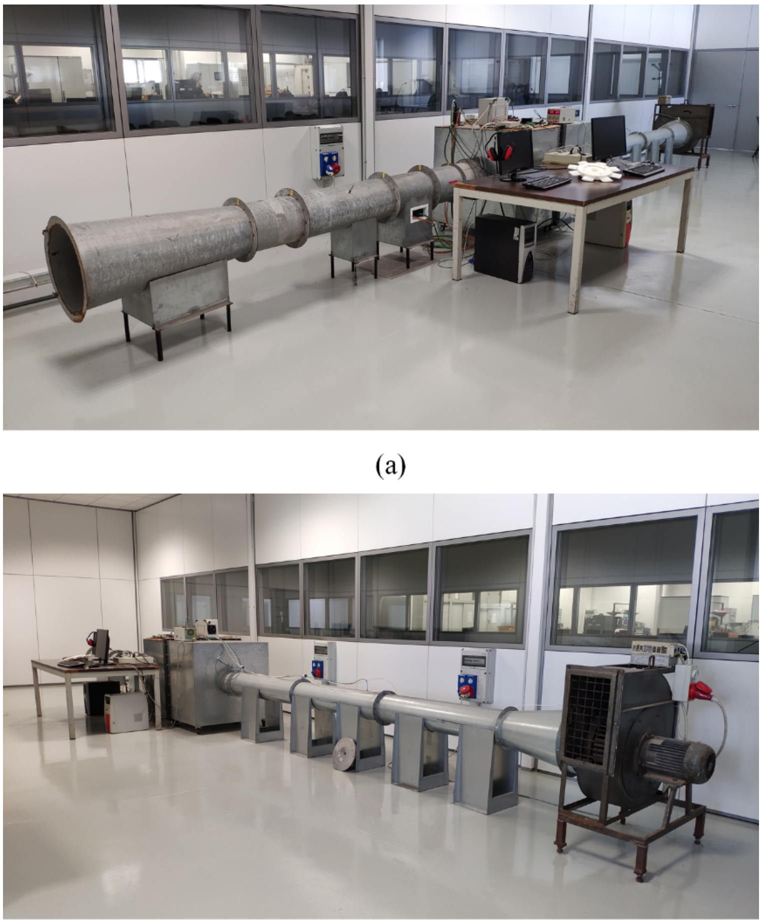

(a)

(b)

Fig. 9. Views of the test rig (GaVe lab at the Polytechnic University of Bari, Italy).

4. Experimental characterization - steady working conditions

As a first step, the Wells turbine has been tested under steady state boundary conditions at 1750 rpm. The performance of the Wells turbine under steady state conditions are reported in figures 10, 11 and 12. Each flow rate is generated by varying the frequency of the control vector drive (hence, the velocity of the blower) up to 60 Hz with steps of 5 Hz. In details, these figures show the experimental T^*, Δp^*, and η, vs. U^*, respectively. As mentioned in the previous section, it is important to note how this test has been carried out by using orifices with different diameter ratios, in order to reduce measurement uncertainty for different flow rates.

Looking at figure 10, it is possible to notice how the turbine is not self-starting. Indeed, the torque coefficient becomes positive only after a determined value of the flow coefficient, i.e. $U^* = 0.07$. Below this value, the machine is driven by the electric motor. As the flow rate, and therefore the flow coefficient, increases, the torque coefficient also increases up to a value close to $T^* = 0.21$ and then drops suddenly due to the stall. In this condition, the flow around the blade profile separates at the so-called static stall angle. The significant performance drop of the turbine is due to higher angles of attack than the stall limit [50].

Moreover, figure 11 highlights the intrinsic characteristic of this type of machine, regarding the stagnation pressure drop. Indeed, the Wells turbine shows a linear correlation of Δp^* in function of U^*. Finally, the efficiency curve in figure 12, shows null values for U^* up to 0.07, then increases as the flow rate increases up to its maximum $\eta = 36.1\%$. After that, stall occurs and the efficiency significantly drops for higher flow rates as the torque coefficient does.

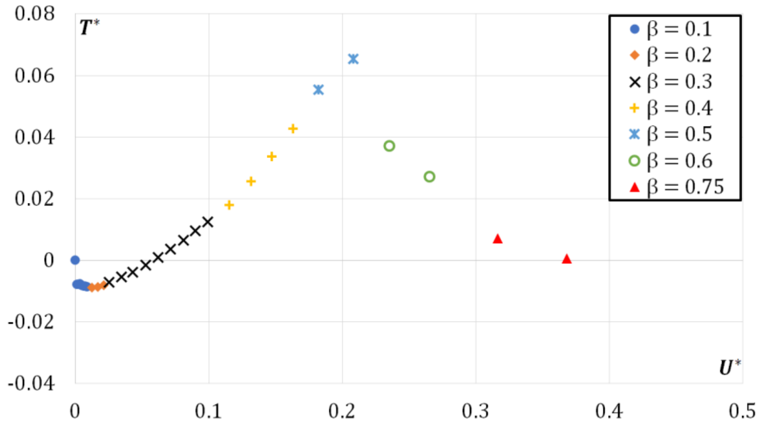

Fig. 10. Steady state experimental curve in terms of torque coefficient T^* vs flow coefficient U^*.

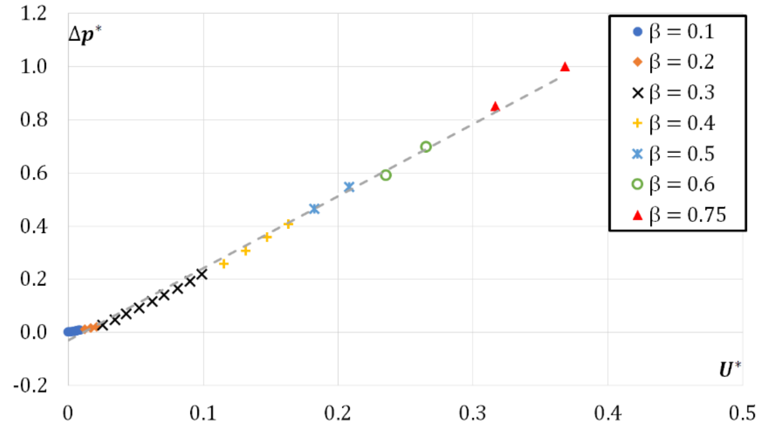

Fig. 11. Steady state experimental curve in terms of stagnation pressure drop Δp^* vs flow coefficient U^*.

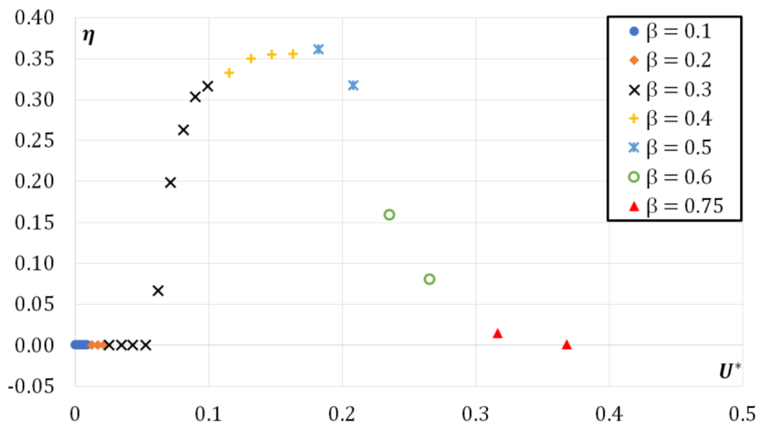

Fig. 12. Steady state experimental curve in terms of stagnation pressure drop η vs flow coefficient U^*

5. Experimental campaign - unsteady working conditions

As previously mentioned in the introduction, several tests have been carried out on the Wells turbine under unsteady flow conditions, with the aim to focus on the effects of amplitude and frequency of the flow rate oscillations on the hysteresis loops in unstalled and deep stall conditions. Actually, in order to replicate flow oscillations such as in the real working conditions of OWC systems, the blower has been driven cyclically with a frequency, f, which changes sinusoidally according to equation 8, for 30 cycles. Indeed, this frequency sinusoidal changing of the frequency involves the same oscillating variation of the flow rate. In addition, the turbine has been tested at 1750 rpm.

$$f(t) = \overline{f} + \Delta f sin(2\pi t/T) \tag{8}$$

The design of experiment (DOE) carried out in this work is represented in the scheme of figure 13. Different values of periods, T, have been considered (i.e., T = 10, 12, 13, 14, 15 and 20 s). In order to evaluate both hysteresis loops in unstalled and deep stall conditions, two mean frequency values, $\overline{f}$, have been selected (i.e., $\overline{f}$ = 20 and 35 Hz). Then, for test identified by each set of T and $\overline{f}$, two frequency amplitude values, Δf, have been considered (i.e., Δf = 10 and 15 Hz). Definitely, 36 tests have been carried out. In order to summarize the results, not all the cases will be shown but only the most interesting in terms of specific working conditions.

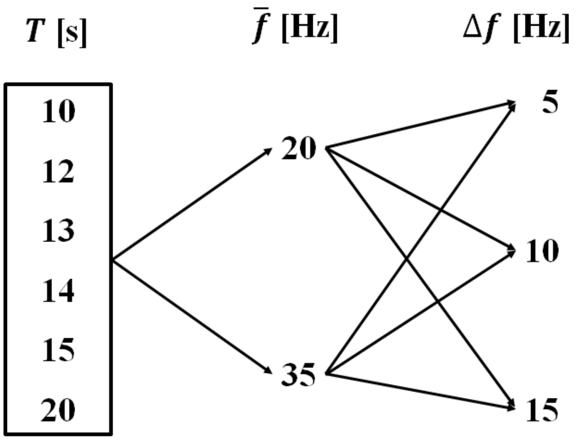

Fig. 13. Design of experiment employed in the experimental campaign.

The reason behind the choice of different periods is related to the objective of understanding what are the operating limits of the machine. Looking at figures 14(a) and 14(b), it is possible to evaluate the time evolution of the mass flow rate, G, for different periods. For the sake of brevity, the comparison has been carried out by keeping constant $\overline{f}$ = 20 Hz and Δf= 15 Hz, and changing the period, T. In figure 14(a), the lowest periods (T = 10 and 12 s) have been compared with the highest one (T = 20 s), in order to better highlight the significant difference between their time evolutions. Indeed, the flow rates acquired at T = 12 and 10 s lose the typical sinusoidal trend, that is expected during normal operating conditions. This can be caused by the delay between the induced flow rate crossing the turbine and the variation of the blower rotational speed. This issue does not happen for the cases at T = 13, 14, 15 and 20 s, as visible in figure 14(b). Then, the period T = 13 s has been selected as the minimum period above which the machine is crossed by a coherent mass flow rate.

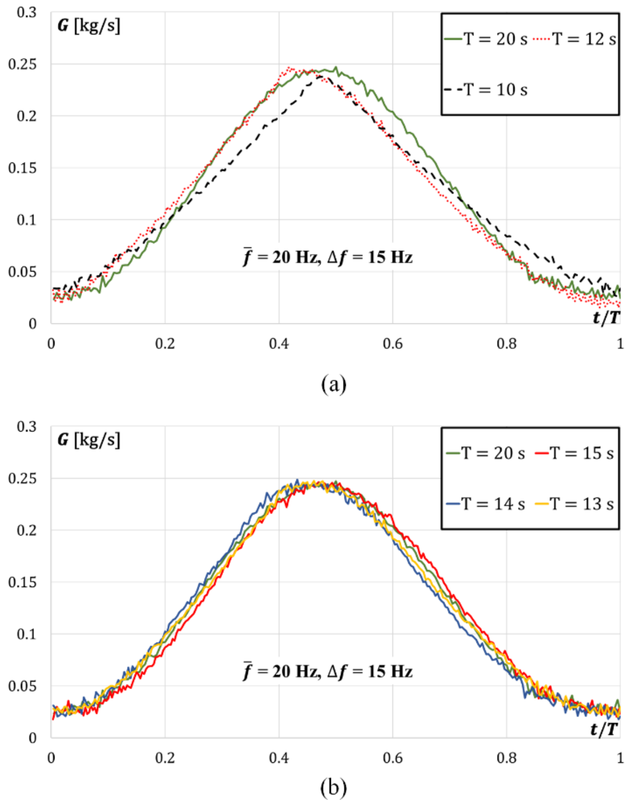

Fig. 14. Comparison of the mass flow rate time evolutions for different periods of the sinusoidal frequency signal sent to the blower. Comparison between T = 10, 12, 20 s (a), and T = 13, 14,15 20 (b) (case $\bar{f}$= 20 Hz, Δf= 15 Hz).

5.1 Effects of the mean frequency $\bar{f}$

Figure 15 shows the clear difference between hysteresis loops under unstalled (15(a)) and deep stall conditions (15(b)). In both the figures, the unsteady curves are compared with respect to the steady state torque coefficient curve. Figure 15(a) shows the typical cycle without stall (case at T = 15 s, $\bar{f}$= 20 Hz, Δf= 15 Hz). It is possible to notice how the unsteady curve is constituted of the upward branch (the dashed red line) and the downward branch (in blue), which follow the steady state curve. Moreover, this curve has been obtained by means a phase averaging over the 30 cycles and no hysteresis loop occurs. Indeed, as reported by Ghisu et al. [51], when the actual angle of attack is lower than the stall angle, the hysteresis cycle is actually due to compressibility within the air chamber (i.e. a phase delay between mass-flow rate variation and piston speed variation) and not by an aerodynamic effect of the turbine.

The unsteady curve in figure 15(b) has been obtained by changing only the mean frequency $\bar{f}$= 35 Hz, keeping unchanged the period and the frequency amplitude with respect to the case of figure 15(a). In this way, the turbine works with larger mass flow rate, reaching and passing the stall condition. This results in a clockwise hysteresis loop, which is due to the different turbine behavior during the acceleration (the dashed red line) and deceleration of the flow (in blue). Particular attention must be paid on what happens once dynamic stall occurs. Indeed, marked damped oscillations emerge and persist during the deceleration phase, postponing the flow reattachment. The amplitude of these oscillations decreases as the flow rate decreases. As results, the machine shows unstable torque coefficients during deceleration phase, due to vortices, which are released from the leading edge, grow and travel over the blade suction side, as reported by McCroskey [52]. The same phenomenon occurs during dynamic stall of a pitching airfoil [53].

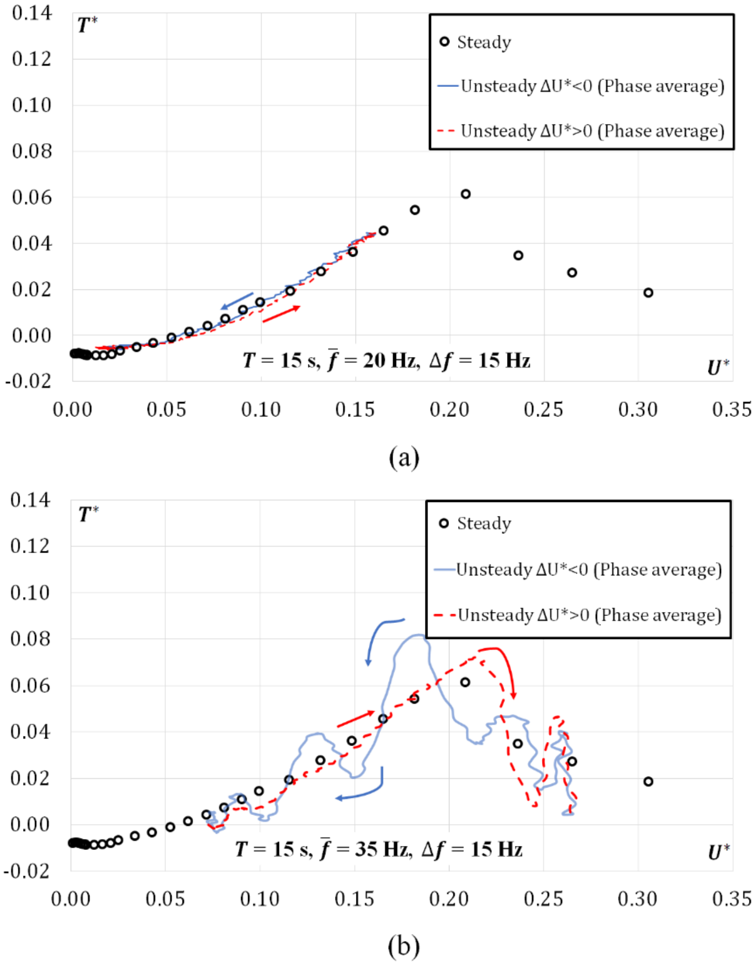

Fig. 15. Torque coefficient T^* vs flow coefficient U^* in unstalled condition (case with T= 15 Hz, $\overline{f}$= 20 Hz, Δf= 15 Hz) (a); and in dynamic stall condition (case with T= 15 Hz, $\overline{f}$= 35 Hz, Δf= 15 Hz) (b).

5.2 Effects of the frequency amplitude Δf

With the aim to focus on the impact of frequency amplitude, Δf, on the turbine performance, two test sets have been selected. For the sake of clarity, the two extreme cases have been selected, i.e. the cases with periods T = 13 and 20 s. Specifically, for each period the comparison has been carried out by keeping constant the mean frequency $\overline{f}$ = 35 Hz, but changing the frequency amplitude (i.e., Δf= 5, 10 and 15 Hz). In details, figures 16 and 17 show the comparison between the time evolution over the period of the torque coefficient at different Δf for T = 20 s and 13 s, respectively. Moreover, each figure shows both T^* curves acquired over 30 cycles and the corresponding phase-averaged values.

Figure 16(a) shows the less stressful working condition with Δf = 5 Hz, highlighted by the sinusoidal trend of T^*. Indeed, the frequency amplitude is not large enough to induce dynamic stall, as it occurs in figure 16(b) and 16(c). These two figures highlight the effect of the stall on the torque coefficient of the turbine. At the beginning, T^* grows regularly up to the stall condition, emphasized with the red circle, which corresponds to the aforementioned U^* = 0.21. Then, T^* starts to show oscillations which are damped up to the end of the period, hence the cycle begins again.

The same considerations can be done looking at figure 17, related to T = 20 s. Additionally, in both cases it is worth to notice how the number of fluctuations increases from Δf = 10 Hz to Δf = 15 Hz. This can be explained by considering the fact that frequency amplitude sent to the vector control drive of the blower increases, while the period in which a single cycle has to be completed remains fixed. This means that the flow rate amplitude has to increase in a shorter period of time, hence the angle of attack changes more quickly. This involves a faster vortex shedding along the suction side of the blades, increasing the number of torque fluctuations. Moreover, focusing on the single curves (not phase-averaged) of the last case (Δf = 15 Hz), it is possible to notice how the T = 13 s case shows larger oscillations at stall with respect to T = 20 s.

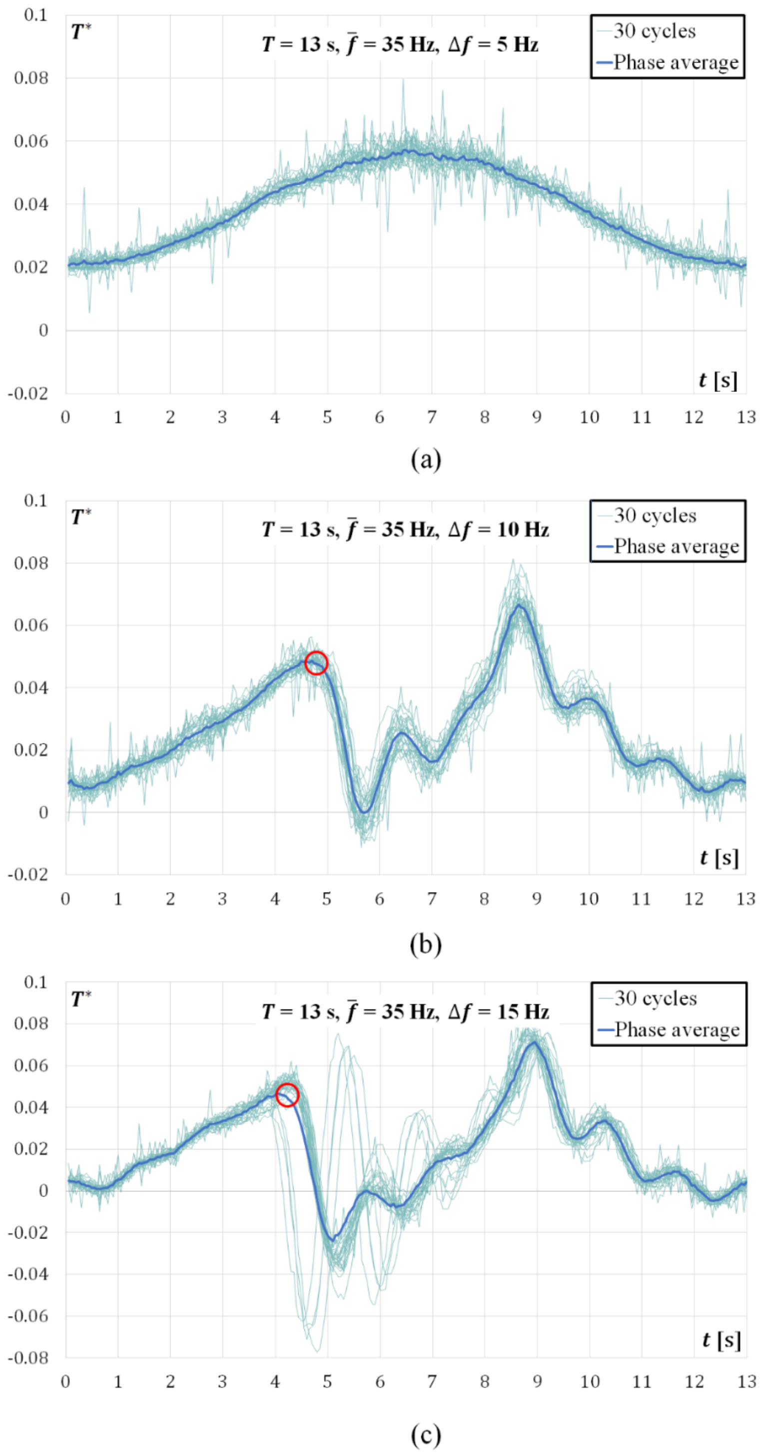

Fig. 16. Effects of the frequency amplitude, Δf, on the time evolution of the torque coefficient (case with T= 13 Hz, $\overline{f}$= 35 Hz and Δf= 5 Hz (a), Δf= 10 Hz (b), Δf= 15 Hz (c)).

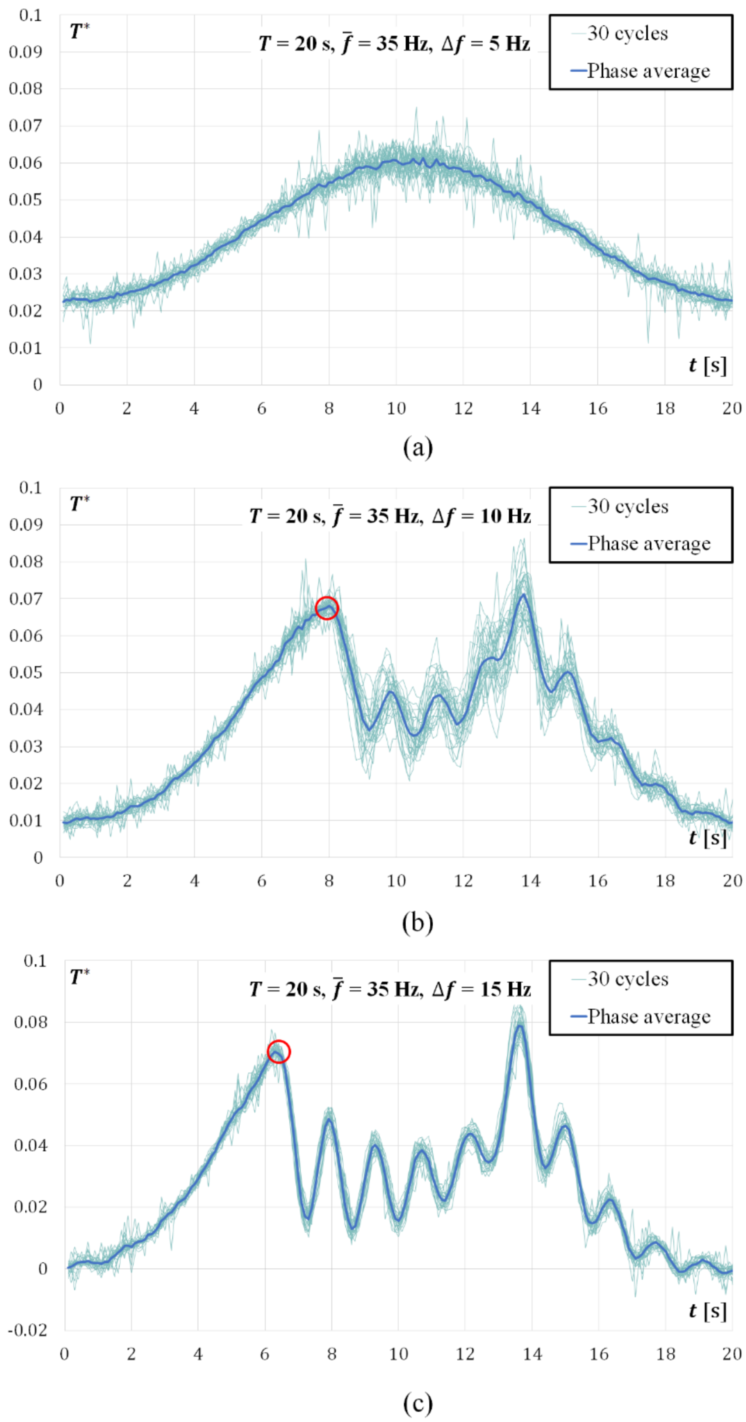

Fig. 17. Effects of the frequency amplitude, Δf, on the time evolution of the torque coefficient (case with T= 20 s, $\overline{f}$= 35 Hz and Δf= 5 Hz (a), Δf= 10 Hz (b), Δf= 15 Hz (c)).

Nevertheless, these torque fluctuations are not due neither to fluctuations of the mass flow rate or the pressure drop coefficient. This is confirmed by looking at figures 18 and 19. Each figure compares the effects of the frequency amplitude variation (Δf from 10 Hz to 15 Hz) on the pressure drop and the flow rate, by keeping constant the mean frequency ($\overline{f}$ = 35 Hz) and the period (T = 13 s in figure 18 and T = 20 s in figure 19).

In both cases, phase-averaged Δp^* curves show a regular and sinusoidal behavior without abnormal fluctuations (see figures 18(a) and 18(b), figure 19(a) and 19(b)). The same considerations can be also applied to the mass flow rate (see figures 18(c) and 18(d), figure 19(c) and 19(d)). For these reasons, they cannot be the cause of the fluctuations present in T^* unsteady curves.

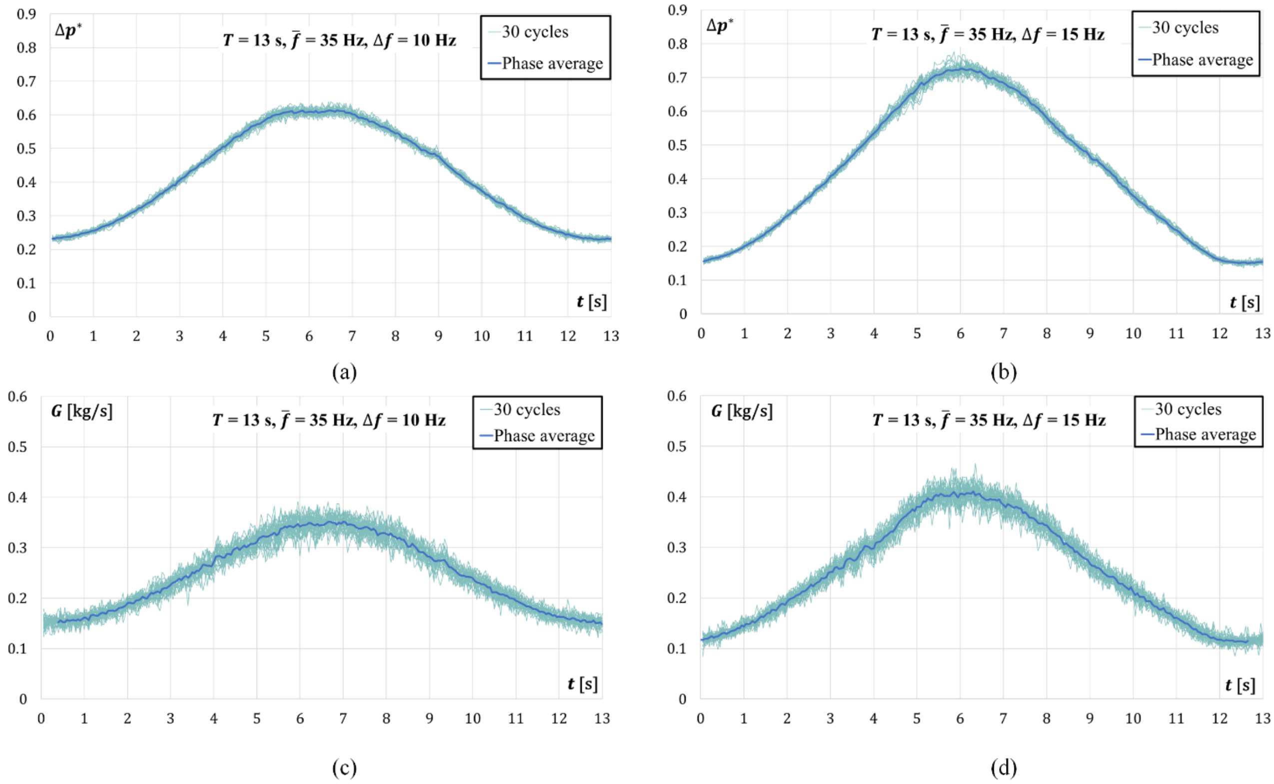

Fig. 18. Phase averaged of the stagnation pressure drop coefficient in no stall condition (a) and dynamic stall condition (b); Phase averaged of the mass flow rate in no stall condition (c) and dynamic stall condition (d) (case with T= 13 s).

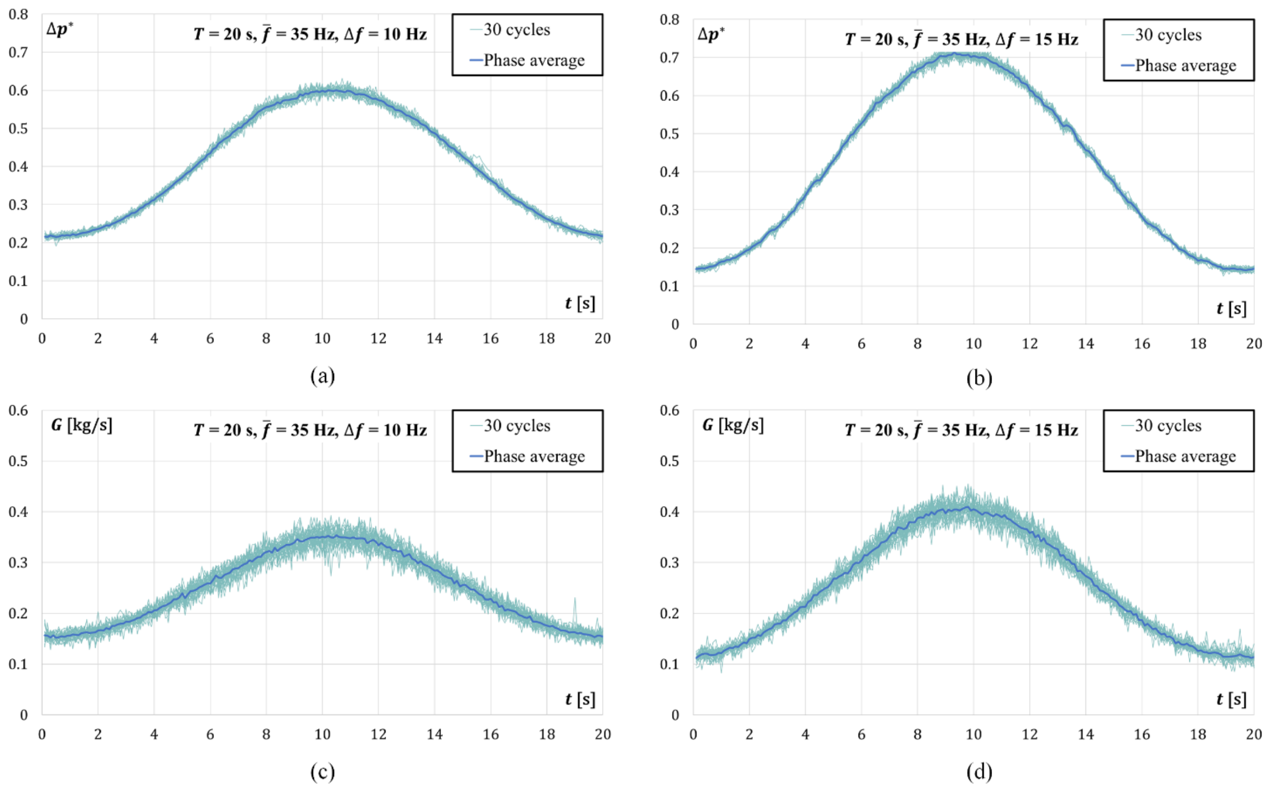

Fig. 19. Phase averaged of the stagnation pressure drop coefficient in no stall condition (a) and dynamic stall condition (b); Phase averaged of the mass flow rate in no stall condition (c) and dynamic stall condition (d) (case with T= 20 s).

5.3 *Effects of the period* T

Figure 20 focuses on the effect of the period, T, on the time evolution of the torque coefficient, T^*, versus time. Since different periods are analyzed, the comparison has been carried out by normalizing the time over the period, t/T. Also in this case, the comparison has been carried out by keeping constant $\overline{f}$ = 35 Hz and Δf (10 Hz in figure 20(a) and 15 Hz in figure 20(b)). Indeed, it is possible to note how the accelerating phase is not affected by any fluctuations up to the stall condition for each period. Regarding this point, T^* curves at 20 s and 15 s reach higher values than the ones at 14 s and 13 s. Then, during the decelerating phase all the T^* curves are characterized by dynamic stall, highlighted by the strong oscillations. Moreover, the amplitude of these oscillations increases as the period decreases (see for example the dotted green line with respect to the red and dashed black ones). In addition, at the lowest period (i.e., 13 s), the curve loses the marked fluctuations, resulting smoother. The increase of Δf from 10 Hz to 15 Hz (see figure 20(b)) involves a greater number of torque fluctuations for the case at 20 s and 15 s with respect to the cases at Δf at 10 Hz in figure 20(a). Instead, also the curve at 14 s seems to be smoother than the one with Δf at 10 Hz in figure 20(a). This can be explained by the higher flow rate that the turbine has to work with in less time.

A confirmation of these effects can be verified by looking at figure 21, where four hysteresis loops under dynamic stall conditions can be compared. Specifically, the comparison regards the more stressful condition, i.e. $\overline{f}$ = 35 Hz, Δf=15 Hz with the other three periods. In all the four cases, the decelerating phase is characterized by strong torque fluctuations triggered once the stall occurs.

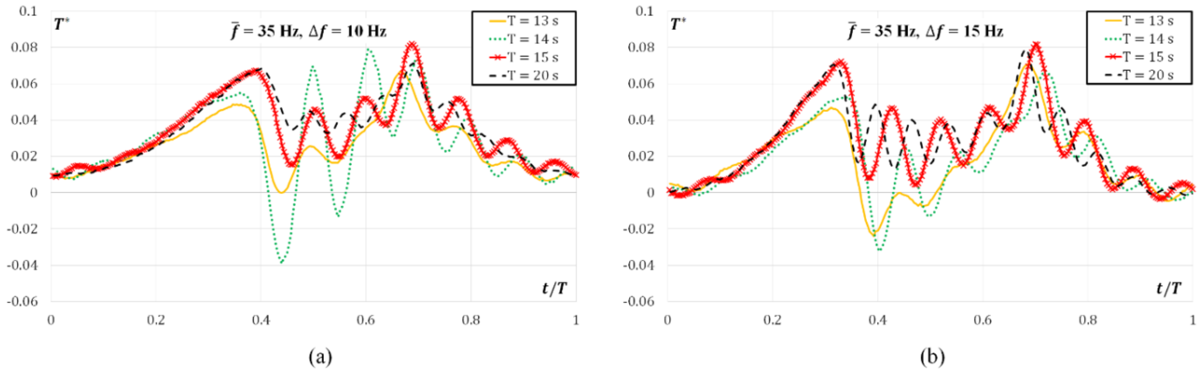

Fig. 20. Effects of the period, T, on the time evolution of the torque coefficient (case with $\overline{f}$= 35 Hz and Δf= 10 Hz) (a), Effects of the period , T, on the time evolution of the torque coefficient (case with $\overline{f}$= 35 Hz and Δf= 15 Hz) (b).

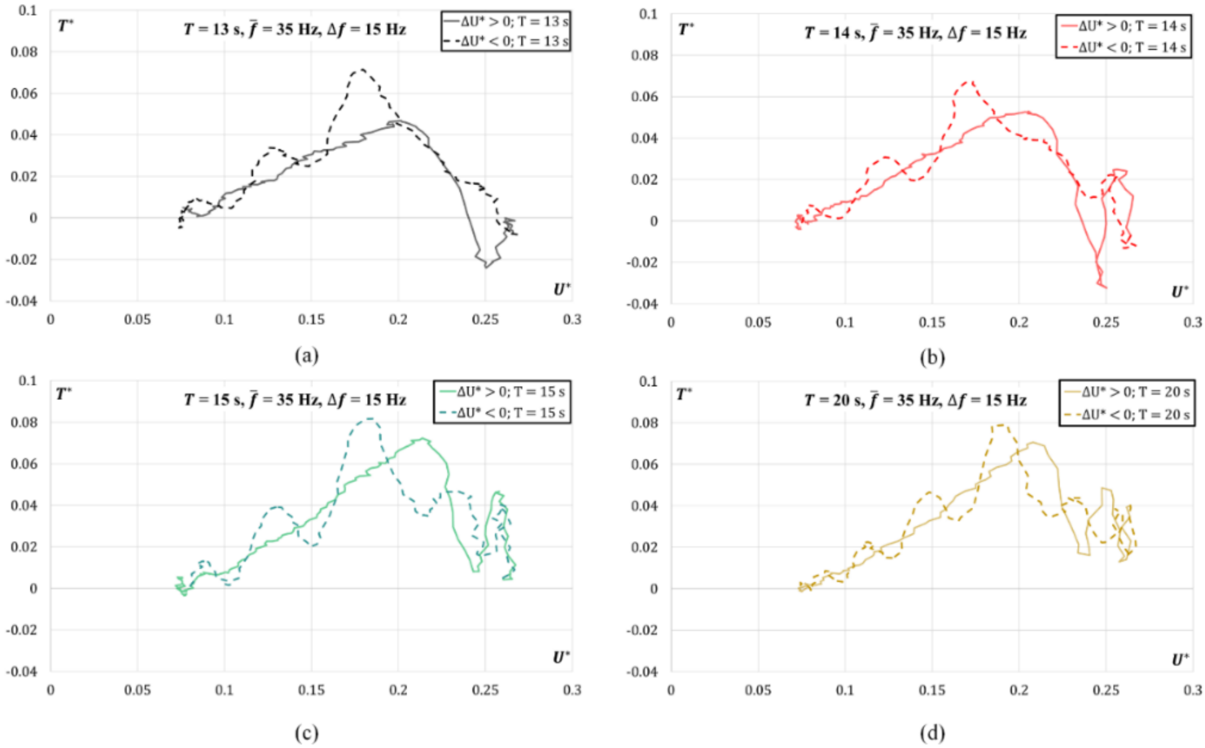

Fig. 21. Comparison between clockwise hysteresis loops for different periods in stall condition.

6. Conclusions

In this work a 3-D printed monoplane Wells turbine has been investigated by carrying out an experimental campaign at the GaVe laboratory of the Polytechnic University of Bari, Italy. The aim of this tests was to investigate the behavior of this new turbine under unsteady flow conditions, especially in terms hysteresis loop during unstalled and dynamic stall conditions.

Indeed, due to the oscillating nature of the flow rate in this kind of applications, Wells turbines are affected by dynamic stall, which has significant effects in terms of performance, vibration, noise and structural integrity of the turbine. Actually, during stall the Wells turbine experiences evident torque fluctuations, which overlay on the typical hysteresis loop, mainly during flow deceleration. The amplitudes of these fluctuations are damped as the flow rate decreases toward reattachment. Often these fluctuations are not evident because hysteresis loops are usually provided with phase-averaged data, which can significantly smoothen or even conceal them.

With the aim to better investigate this phenomenon, this work proposes a new 3D-printed monoplane Wells turbine, which has been tested at the open wind tunnel of the Polytechnic University of Bari, Italy. The interest is mainly focused on the effects of frequency and amplitude of the oscillating flow rate on the performance of the machine.

In order to replicate typical unsteady working conditions in OWC systems, an unidirectional sinusoidal oscillating flow has been generated by varying the frequency signal sent to the vector control drive of the blower.

The machine has been firstly investigated in steady state, then under dynamic stall working conditions. A total of 36 tests have been carried out by changing the three main parameters, which characterize the oscillating flow (i.e., the period, the mean frequency and the amplitude of the frequency signal sent to the vector control drive).

The first study has been focused on finding out the period below which the flow rate does not follow the sinusoidal trend imposed by the blower (i.e., T = 13 s). Then, a series of analyses has been carried out in order to evaluate the effect of a parameter, by keeping constant the other ones.

Increasing the mean frequency or the frequency amplitude involves the machine working towards stall condition, due to the increase of the flow rate. In addition, during dynamic stall, the shaft torque experiences damped fluctuations at frequencies higher than that of the main flow. This phenomenon happens during the flow deceleration and the flow reattachment and it is intensified as the amplitude of the oscillating flow rate increases and the wave period decreases.

Moreover, it has been found out how this unsteady behavior is not caused by both the mass flow rate crossing the turbine and the stagnation pressure drop. Indeed, these two performance parameters does not show perturbations or fluctuations over the period, resulting in sinusoidal trend, as imposed by the blower. For this reason, these torque fluctuations during dynamic stall conditions are related to the detachment of vortices generated from the leading edge and travelling along the suction side of the blade. Finally, detecting these oscillations can be relevant in the turbine design phase to enhance the structural strength of the Wells turbine.

Acknowledgements

This work was carried out under the Programme: "Department of Excellence" Legge 232/2016 (Grant No. CUP-D94I18000260001) supported by MIUR-"Ministero dell'Istruzione dell'Università e della Ricerca".

Funding

This research did not receive any specific grant from funding agencies in the public, commercial, or not-for-profit sectors.

Nomenclature

Symbols

c	Blade chord [m]
D	Diameter [m]
f	Frequency [Hz]
G	Mass flow rate [kg/s]
h	Hub-to-tip ratio [-]
N_b	Number of blades [-]
P	Power [W]
R_{hub}	Hub radius [m]
R_{tip}	Tip radius [m]
s	Solidity [-]
T	Period [s]
T^*	Torque coefficient [-]
V	Air axial velocity [m/s]
Δf	Frequency amplitude [Hz]
Δp^*	Stagnation pressure drop coefficient [-]

Greek letters

β	Orifice diameter ratio [-]
η	Efficiency [-]
ρ	Density [kg/m^3]
ω	Angular velocity [rad/s]

Abbreviations

CFD	Computational Fluid Dynamic
DOE	Design Of Experiment
LCOE	Levelized Cost of Energy
OWC	Oscillating Water Column
PTO	Power Take-Off
SCADA	Supervisor Control and Data Acquisition
TRL	Technology Readiness Level

References

[1] IRENA, World Energy Transitions Outlook: 1.5°C Pathway, International Renewable EnergyAgency, Abu Dhabi, 2021

[2] International Energy Agency (IEA). Global Energy & CO_2 Status Report 2019; IEA: Paris, France, 2019

[3] International Energy Agency (IEA). Global Energy Review 2020—The Impacts of the COVID-19 Crisis on Global Energy Demand and CO_2 Emissions; IEA: Paris, France, 2020.

[4] IEA (2021), World Energy Outlook 2021, IEA, Paris, 2021. https://www.iea.org/reports/world-energy-outlook-2021

[5] UN Climate change conferene UK 2021. Url: https://ukcop26.org/cop26-goals/

[6] T. Capurso, M. Stefanizzi, M. Torresi, S.M. Camporeale, Perspective of the role of hydrogen in the 21st century energy transition, Energy Conversion and Management 251 (2022) 114898. https://doi.org/10.1016/j.enconman.2021.114898

[7] M. Stefanizzi, T. Capurso, G. Filomeno, M. Torresi, G. Pascazio, Recent Combustion Strategies in Gas Turbines for Propulsion and Power Generation toward a Zero-Emission Future: Fuels, Burners, and Combustion Techniques, energies 14(20) (2021) 6694. https://doi.org/10.3390/en14206694

[8] IRENA, Renewable capacity highlights, 2021.
[9] IRENA, Offshore renewables: An action agenda for deployment, International Renewable Energy Agency, Abu Dhabi.
[10] G. Mørk, S. Barstow, A. Kabuth, M. Pontes, "Assessing the Global Wave Energy Potential" in Proceedings of the 29th International Conference on Ocean, Offshore and Arctic Engineering, 3 (ASME, 2010), pp. 447–454.
[11] S. Astariz, G. Iglesias, The economics of wave energy: A review, Renewable and Sustainable Energy Reviews 45 (2015) 397-408. https://doi.org/10.1016/j.rser.2015.01.061.
[12] European Union Commission, An EU Strategy to harness the potential of offshore renewable energy for a climate neutral future , 2020. https://ec.europa.eu/energy/sites/ener/files/offshore_renewable_energy_strategy.pdf
[13] Ocean Energy Europe, 2030 Ocean Energy Vision – Industry analysis of future deployments, cost and supply chains, 2020. https://www.oceanenergy-europe.eu/wp-content/uploads/2020/10/OEE_2030_Ocean_Energy_Vision.pdf
[14] Ocean Energy Europe, Ocean Energy – Key trends and statistics 2020, 2021. https://www.oceanenergy-europe.eu/wp-content/uploads/2021/03/OEE-Stats-Trends-2020.pdf.
[15] M.A. Mustapa, O.B. Yaakob, Y.M. Ahmed, C.K. Rheem, K.K. Koh, F.A. Adnan, Wave energy device and breakwater integration: A review, Renewable and Sustainable Energy Reviews 77 (2017) 43-58. https://doi.org/10.1016/j.rser.2017.03.110.
[16] S. Raghunathan, The wells air turbine for wave energy conversion, Progress in Aerpospace Sciences 31(4) (1995) 335-386. https://doi.org/10.1016/0376-0421(95)00001-F.
[17] Ocean Wave Energy Systems – Hydrodynamics, Power Takeoff and Control Systems, Springer (2022) https://doi.org/10.1007/978-3-030-78716-5.
[18] E. Medina-Lopez, N.W.H. Allsop, A. Dimakopolus, T. Bruce, Conjectures on the failure of the OWC Breakwater at Mutriku, In Proceedings of Coastal Structures and Solutions to Coastal Disasters Joint Conference, Boston, Massachusetts (2015).
[19] Y. Torre-Enciso, I. Ortubia, L.I. López de Aguileta, J. Marqués, Mutriku wave power plant: from the thinking out to the reality. In Proceedings of the 8th European Wave and Tidal Energy Conference, Uppsala, Sweden (2009), 19329.
[20] Wikipedia, Mutriku Breakwater Wave Plan. Url https://en.wikipedia.org/wiki/Mutriku_Breakwater_Wave_Plant [online, access on 20/07/2022].
[21] Offshore energy, Mutriku Wave Plant Hits 2 GWh Mark. Url: https://www.offshore-energy.biz/mutriku-wave-plant-hits-2gwh-mark/ [online, access on 20/07/2022].
[22] A.F.O. Falcão, J.C.C. Henriques, Oscillating-water-column wave energy converters and air turbines: A review, Renewable Energy 85 (2016), 1391-1424. https://doi.org/10.1016/j.renene.2015.07.086.
[23] R. Abassi, M.J. Ketabdari, Enhancement of OWC Wells turbine efficiency and performance using riblets covered blades, a numerical study, Energy Conversion and Management 254 (2022) 1152212. https://doi.org/10.1016/j.enconman.2022.115212.
[24] L.M.C. Gato, V. Warfield, A. Thakker, Performance of a High-Solidity Wells Turbine for an OWC Wave Power Plant, Journal of Energy Resources Technology 118(4) (1996) 263-268 . https://doi.org/10.1115/1.2793872.
[25] M. Takao, K. Takasaki, S. Okuhara, T. Setoguchi, Wells turbine for wave energy conversion- improvement of stall characteristics by the use of 3-dimensional blades, Journal of Fluid Science and Technology 9 (2014) 1–7. https://doi.org/10.1299/jfst.2014jfst0052.
[26] M. Torresi, S. M. Camporeale, P.D. Strippoli, G. Pascazio, Accurate numerical simulation of a high solidity Wells turbine, Renewable Energy 33 (2008) 735-747. https://doi.org/10.1016/j.renene.2007.04.006.
[27] A.T.M. Kotb, M.A.A. Nawar, R.A. El Maksoud, Y.A. Attai, M.H. Mohamed, Potential of performance improvement of a modified Wells turbine using passive control for wave energy conversion, Ocean Engineering 242 (2021) 110178. https://doi.org/10.1016/j.oceaneng.2021.110178.
[28] K. Geng, C. Yang, C. Hu, Y. Li, C. Yang, Numerical investigation on the loss audit of Wells turbine with exergy analysis, Renewable Energy 189 (2022) 273-287. https://doi.org/10.1016/j.renene.2022.02.042.
[29] L. Ciappi, L. Cheli, I. Simonetti, A. Bianchini, L. Talluri, L. Cappietti, G. Manfrida, Wave-to-wire models of wells and impulse turbines for oscillating water column wave energy converters operating in the Mediterranean Sea, Energy 238 (2022) 121585. https://doi.org/10.1016/j.energy.2021.121585.
[30] L. Ciappi, L. Cheli, I. Simonetti, A. Bianchini, G. Manfrida, L. Cappietti, Wave-to-wire models of Oscillating-Water-Column Wave Energy Converters and Its Applications to Mediterranean Energy Hot-Spots, Energies 13(21) (2020) 5582. https://doi.org/10.3390/en13215582.
[31] L. Gurnari, P.G.F. Filianoti, M. Torresi, S.M. Camporeale, The Wave-to-Wire Energy Conversion Process for a Fixed U-OWC Device, Energies 13(1) (2020) 283. https://doi.org/10.3390/en13010283.
[32] S. Shaaban, A.A. Hafiz, Effect of duct geometry on Wells turbine performance, Energy Conversion and Management 61 (2012) 51-58. https://doi.org/10.1016/j.enconman.2012.03.023.
[33] J.S. Alves, L.M.C. Gato, A.F.O. Falcão, J.C.C. Henriques, Experimental investigation on performance improvement by mid-plane guide-vanes in a biplane-rotor Wells turbine for wave energy conversion, Renewable and Sustainable Energy Reviews 150 (2021) 111497. https://doi.org/10.1016/j.rser.2021.111497.

[34] A. Mahrooghi, E. Lakzian, Optimization of Wells turbine performance using a hybrid artificial neural fuzzy inference system (ANFIS) - Genetic algorithm (GA), Ocean Engineering 226 (2021) 108861. https://doi.org/10.1016/j.oceaneng.2021.108861.

[35] R. Starzmann, T. Carolus, Effect of Blade Skew Strategies on the Operating Range and Aeroacoustic Performance of the Wells Turbine, Journal of Turbomachinery 136(1) (2014) 011003. https://doi.org/10.1115/1.4025156 .

[36] P.M. Kumar, P. Halder, A. Husain, A. Samad, Performance enhancement of Wells turbine: Combined radiused edged blade tip, static extended trailing edge, and variable thickness modifications. Ocean Engineering 185 (2019) 47-58. https://doi.org/10.1016/j.oceaneng.2019.05.041.

[37] M. Paderi, P. Puddu, Experimental investigation in a Wells turbine under bidirectional flow, Renewable Energy 57 (2013) 570-576.

[38] P. Puddu, M. Paderi, C. Manca, Aerodynamic characterization of a Wells turbine under bi-directional airflow, Energy Procedia 45 (2014) 278-287.

[39] T. Setoguchi, Y. Kinoue, T.H. Kim, K. Kaneko, M. Inoue, Hysteretic characteristics of Wells turbine for wave power conversion, Renewable Energy 28(13) (2003) 2113-2127

[40] A. Thakker, R. Abdulhadi, Effect of blade profile on the performance of wells turbine under unidirectional sinusoidal and real sea flow conditions, International Journal of Rotating Machinery (2007) 51598.

[41] A. Thakker, R. Abdulhadi, The performance of Wells turbine under bi-directional airflow, Renewable Energy 33(11) (2008) 2467-2474.

[42] T.H. Kim, Y. Kinoue, T. Setoguchi, K. Kaneko, Effects of hub-to-tip ratio and tip clearance on hysteretic characteristics of wells turbine for wave power conversion, Journal of Thermal Science 11(3) (2002) 207-213.

[43] T. Setoguchi, Y. Kinoue, M. Moharnrnad, K. Kaneko, M. Takao, Unsteady flow phenomena of Wells turbine in deep stall condition, In Proceedings of the 14th International Offshore and Polar Engineering Conference, Toulon, France (2004), 266-271.

[44] Y. Kinoue, T. Setoguchi, T.H. Kim, M. Mammum, K. kanekko, M. Inoue, Hysteretic characteristics of the Wells turbine in a deep stall condition, In Proceedings of the Institution of Mechanical Engineers, Part M: Journal of Engineering for the Maritime Environment 218(3), 167-173.

[45] T. Ghisu. P. Puddu, F. Cambuli, Physical explanation of the hysteresis in Wells turbines: A critical reconsideration, Journal of Fluids Engineering 138 (11) (2016) 1-9.

[46] F. M'zoughi, I. Garrido, A.J. Garrido, M. De La Sen, Rotational Speed Control Using ANN-Based MPTT for OWC Based on Surface Elevation Measurement, Applied Sciences 10(24) (2020), 8975. https://doi.org/10.3390/app10248975 .

[47] S.M. Camporeale, P.G.F. Filianoti, Energy Conversion of OWC devices with additional vertical ducts, Proceedings of the 27th International Conference of Offshore Mechanics and Arctic Engineering (2008), 739-750. https://doi.org/10.1115/OMAE2008-57769

[48] M. Torresi, M. Stefanizzi, L. Gurnari, P.G.F. Filianoti, S.M. Camporeale, Experimental characterization of the unsteady performance behavior of a Wells Turbine operating at high flow rate coefficients, E3S Web of Conferences 197 (2020) 08009. https://doi.org/10.1051/e3sconf/202019708009.

[49] M. Torresi, M. Stefanizzi, F. Fornarelli, L. Gurnari, P.G.F. Filianoti, S.M. Camporeale, Performance characterization of a Wells turbine under unsteady flow conditions, AIP Conference Proceedings 2191 (2019) 020149. https://doi.org/10.1063/1.5138882.

[50] R.E. Sheldahl, P.C. Klimas, Aerodynamic characteristics of seven symmetrical airfoil sections through 180-degree angle of attack for use in aerodynamic analysis of vertical axis wind turbines, Sandia National Laboratories Energy Report (1981). https://doi.org/10.2172/6548367.

[51] T. Ghisu, F. Cambuli, P. Puddu, I. Virdis, M. Carta, F. Licheri, A lumped parameter model to explain the cause of the hysteresis in OWC-Wells turbine systems for wave energy conversion, Applied Ocean Research 94 (2020) 101994. https://doi.org/10.1016/j.apor.2019.101994.

[52] W.J. McCroskey, The phenomenon of dynamic stall, Tech. Rep., Natl. Aeronaut. Space Admin. (1981), Washington, DC.

[53] M. Torresi, E. De Tomaso, B. Fortunato, S.M. Camporeale, G. Pascazio, High frequency dynamics of force coefficients in VAWT blades under dynamic stall condition, in the Proceedings of ASME Turbo Expo 2015: Power for Land, Sea and Air, (2015), GT2015-42987. https://doi.org/10.1115/GT2015-42987.